ACS OMEGA

Open Access

http://pubs.acs.org/journal/acsodf

Article

Mechanism Behind the Enhanced Ferromagnetic Contributions Upon Ru Substitution in $Ca_3Mn_2O_7$ from X-Ray Absorption Spectroscopies

Gloria Subías,* Vera Cuartero, Javier Herrero-Martín, Sara Lafuerza, Viktoriia A. Saveleva, Pieter Glatzel, Raffaella Torchio, Olivier Mathon, and Javier Blasco*

Cite This: *ACS Omega* 2024, 9, 41396−41407

Read Online

ACCESS | Metrics & More | Article Recommendations | Supporting Information

ABSTRACT: We have studied the local structure and electronic and magnetic properties of hybrid improper ferroelectric $Ca_3Mn_2O_7$ upon Ru substitution at the Mn site by a combination of atomic-selective X-ray absorption spectroscopies in the soft and hard X-ray energy regimes. Ru substitution enhances the macroscopic ferromagnetic contributions, whose origin is here elucidated. In particular, soft X-ray magnetic circular dichroism (XMCD) data indicate that the spin moments of Mn and Ru are aligned in opposite directions, with the effective magnetic moments of Ru being about 1 order of magnitude smaller than for Mn. The XMCD results also demonstrate the presence of an intrinsic ferromagnetic component in the Mn sublattice for Ru contents $x \geq 0.3$, although the values of the net Mn magnetic moment are much smaller than expected for a fully saturated Mn^{4+} magnetic sublattice. Soft and hard X-ray absorption spectroscopy measurements show that Mn keeps a +4 valence state independently of the Ru content, whereas Ru is in an intermediate valence state, ranging between +4.7 ($x \leq 0.1$) and +4.4 ($x \geq 0.7$). Analysis of the extended X-ray absorption fine structure (EXAFS) signals at the Mn and Ru K-edges suggests the lack of a complete solid solution in the local structure across the entire range of compositions. These findings disclose the existence of charge transfer between Mn and Ru atoms, so the weak ferromagnetic component is attributed to a canting of the antiferromagnetically ordered Mn^{4+} spins caused by the oxygen-mediated hybridization between localized Mn^{4+} 3d and itinerant intermediate valence Ru 4d bands, in analogy to the mechanism proposed for ferromagnetism in ordered doubled perovskites with 3d and 4d/5d transition-metal ions. In the present case, disorder prevents the formation of long-range ferromagnetism.

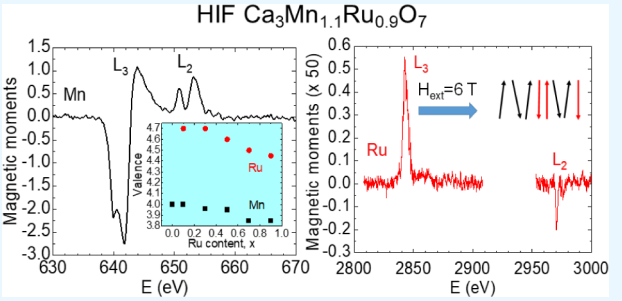

INTRODUCTION

Layered perovskite oxides are a scientifically and technologically important class of materials because they show functionalities beyond those of the simple ABO_3 perovskites. Of particular interest is the $A_{n+1}B_nO_{3n+1}$ Ruddlesden−Popper (RP) family with $n = 2$, where electric polarization arises from the combination of coherent rotations and tilting of BO_6 octahedra that break inversion symmetry, yielding a net polarization. Materials showing this mechanism are known as hybrid improper ferroelectrics (HIFs).[1] So far, switchable ferroelectric polarization has been demonstrated experimentally in a number of nonmagnetic HIF RP phases, including $(Ca,Sr)_3Ti_2O_7$,[2] low-Mn-doped $Ca_3Ti_2O_7$,[3] or $Sr_3Sn_2O_7$.[4] The next step toward the realization of multiferroicity in this class of materials is the design of HIF magnets, in which (anti)ferromagnetism and ferroelectricity are induced through the same lattice instability. In this way, a direct and strong coupling between polarization and magnetism could be realized, expanding the functionality of these materials. In particular, $Ca_3Mn_2O_7$ has been proposed by Benedek and Fennie[1] as the prototype of this class of magnetoelectric materials. $Ca_3Mn_2O_7$ shows a structural transition at $T_S \sim 310$ K from a tetragonal $I4/mmm$ phase, consisting of alternating CaO layers and $CaMnO_3$ bilayers along the c axis, to a polar orthorhombic phase $A2_1am$. Here, the polar mode is driven by the combination of the two nonpolar MnO_6 octahedra distortions, a rotation around the [001] direction, and a tilting around the [110] axis. Moreover, the Mn^{4+} moments undergo an antiferromagnetic (AFM) ordering[5] of G-type at $T_N = 112$ K, and the net magnetization exhibits weak ferromagnetism below T_N, which can be modulated by the electric field.[6] The MnO_6 octahedral tilting supports these canted spin moments through the Dzyaloshinskii−Moriya interaction. However, the

Received: May 7, 2024
Revised: August 29, 2024
Accepted: September 3, 2024
Published: September 25, 2024

Néel temperature of this material is still low, which prevents its use for room temperature technological applications.

In order to further tune the functional properties of $Ca_3Mn_2O_7$ toward multiferroicity at room temperature, previous studies mainly focused on A-site doping to realize the transformation from AFM to ferromagnetic (FM) ordering.[7−9] The AFM Néel temperature was slightly increased from 112 to 130 K in La-doped $Ca_3Mn_2O_7$[7] while only weak ferromagnetism was achieved by Li doping.[8] In parallel to the one-electron-doped $Ca_{3-x}La_xMn_2O_7$ series, two-electron doping with tetravalent Th at the Ca site also induces a significant FM component at $x = 0.05$, which diminishes with a further increase of x and completely disappears at $x = 0.2$. On the other hand, B-site doping was less studied.[10,11] Ru substitution enhances the Curie temperature in RP $La_{1.2}Ca_{1.8}Mn_{2-x}Ru_xO_7$ compounds even though the total magnetization decreases.[10] This was understood in terms of the AFM coupling between high-spin-average Mn $3d^{3.6}$ and Ru $4d^{4.6}$ configurations. On the other hand, it was recently found that AFM interactions were weakened in low-doped $Ca_3Mn_{2-x}Ru_xO_7$ ($x \leq 0.1$) samples when prepared by the sol−gel method, and at the same time that the Neel temperature slightly increases up to around 120 K.[11] The enhancement of ferromagnetism in this case was associated with the replacement of Mn^{4+} by Ru^{3+}, leading to the appearance of Mn^{3+} and oxygen vacancies that break the superexchange Mn^{4+}−O−Mn^{4+} interactions. Finally, Ru substitution in the related HIF $Ca_3Ti_2O_7$[12] reduces the coercive electric field while it induces weak ferromagnetism. This behavior was ascribed to the increase of oxygen vacancies (and concentration of Ti^{3+}) upon Ru^{4+} doping, which leads to the development of spin-polarized Ru^{4+} 4d orbitals in a low spin configuration (t_{2g}^4).

The association of manganese and ruthenium in the same perovskite matrix is of great interest in promoting FM ordering, since Ru^{4+} and Ru^{5+} species exhibit d^4 and d^3 electronic configurations, respectively, formally equivalent to those in Mn^{3+} and Mn^{4+}, which can induce a double exchange Mn^{3+}−O−Mn^{4+} mechanism for ferromagnetism. We prepared the $Ca_3Mn_{2-x}Ru_xO_7$ series in a very broad compositional range ($0 \leq x \leq 0.9$) by solid-state synthesis. The structural and magnetic properties were characterized by neutron powder diffraction (NPD).[13] All samples were single phase and showed the same polar orthorhombic $A2_1am$ crystal structure of the parent compound $Ca_3Mn_2O_7$ at room temperature regardless of the Ru content. So, from a structural point of view, the HIF mechanism is retained along the whole $Ca_3Mn_{2-x}Ru_xO_7$ series. The analyses of NPD data proved that the long-range magnetic ordering is AFM in all samples. However, the ground state varies with the Ru content. A G-type magnetic ordering is found for $x \leq 0.1$ while an A-type component appears for $x \geq 0.3$.[13] The macroscopic magnetic study revealed the occurrence of tiny remanent magnetization in the hysteresis loops for Ru contents $x \geq 0.3$ at low temperatures below T_N. This indicates that a high enough Ru incorporation into the Mn sites in $Ca_3Mn_2O_7$ induces a FM component, which is however rather faint, since it was not detectable by neutron diffraction.[13] This weak FM component is also detectable at temperatures above T_N, but with a strong decrease of coercivity.

To elucidate the origin of the enhanced FM contributions in the $Ca_3Mn_{2-x}Ru_xO_7$ ($0 \leq x \leq 0.9$) series, we have examined the local electronic and magnetic properties and also the geometrical local structure of Mn and Ru atoms via complementary soft and hard X-ray absorption spectroscopies. In particular, Mn and Ru $L_{2,3}$ X-ray magnetic circular dichroism (XMCD) was collected in total electron yield (TEY) mode, recording the sample drain current. We have exploited the sensitivity of XMCD at the $L_{2,3}$ edges of 3d and 4d transition metal atoms to the magnetic moments with atomic selectivity and to the exact magnetic coupling (parallel or antiparallel) between the Mn and Ru atoms. The combination of the results from the XMCD analysis with the macroscopic magnetic response[13] has allowed us to distinguish how these two atoms contribute to the FM correlations. To quantify the valence state of Mn and Ru atoms, X-ray absorption near edge spectroscopy (XANES) spectra were recorded in both the transmission mode across the Mn and Ru K edges (1s→4p dipolar transitions) and the TEY mode at the $L_{2,3}$ edges (2p→3d (Mn)/4d (Ru) dipolar transitions). In the latter, the 3d(4d) electrons of Mn(Ru) atoms are directly probed, but the correlation between the spectral shape and the oxidation state of the absorbing species is not always straightforward. Furthermore, TEY-detected XANES measurements are surface-sensitive. Ru L_3 XANES measurements were additionally obtained in the high-energy resolution fluorescence detected (HERFD) mode,[14] using a specific decay channel, which allowed covering the lowest Ru concentrations ($x \leq 0.1$). On the other hand, Mn and Ru K-edge XANES measurements are bulk-sensitive and they are sensitive to the valence state through the threshold position of the absorption edge, which shifts to higher energy with increasing metal valence.[15] Finally, the local geometrical structure around both atoms has been determined by analyzing the extended X-ray absorption fine structure (EXAFS) signals at the Mn and Ru K-edges, respectively.

EXPERIMENTAL DETAILS

Polycrystalline $Ca_3Mn_{2-x}Ru_xO_7$ ($x = 0$, 0.05, 0.1, 0.3, 0.5, 0.7, 0.9) samples were prepared by the solid-state reaction of Mn_2O_3, $CaCO_3$, and RuO_2 precursor powders as reported in ref 13. These samples were previously characterized by powder X-ray diffraction (XRD) measurements with a Rigaku D-Max system using Cu $K_{\alpha 1,2}$ wavelengths, which confirmed that they are single phase. The chemical composition was analyzed by using the wavelength dispersive X-ray fluorescence spectrometry technique, and all the samples showed the nominal stoichiometry. NPD confirmed the polar orthorhombic $A2_1am$ crystal structure and long-range AFM ordering for all the samples used in this study.[13]

TEY-detected XANES and XMCD measurements at the Mn-$L_{2,3}$ (630−670 eV) and the Ru-$L_{2,3}$ (2800−3000 eV) edges were performed at the HECTOR cryomagnet end station in the BL29 BOREAS beamline[16] of the ALBA synchrotron radiation facility in Barcelona, Spain. At Mn-$L_{2,3}$, the photon flux was about 1012 ph/s with an energy resolution of ∼50 meV, with the degree of circular polarization being >99%. At Ru $L_{2,3}$, the flux was $\sim 5 \times 10^9$ ph/s, the energy resolution was 1.4 eV, and the degree of circular polarization delivered by the Apple II-type elliptical undulator was adjusted to 70% as a necessary trade-off with photon flux when working at high photon energies requiring the use of high undulator harmonics.

Sintered pellets were prepared for the TEY-detected XANES and XMCD measurements, which were also cleaved in situ under ultrahigh vacuum conditions (∼10^{-9} mbar) to obtain

https://doi.org/10.1021/acsomega.4c04334
ACS Omega 2024, 9, 41396−41407

clean sample surfaces. The XMCD signals were obtained by subtracting the XANES recorded using circular polarization with positive and negative helicities (μ_+ and μ_-, respectively) under a magnetic field of 6 T applied parallel to the beam propagation direction (or under no applied field). In all cases, the samples were kept at a temperature of 50 K. The XMCD spectra have then been normalized by dividing by the maximum at the L_3 of the corresponding XANES sum spectrum:

$$\mathrm{XMCD}(E) = \frac{\mu_+(E) - \mu_-(E)}{\mu_+(L_3) + \mu_-(L_3)}$$

To minimize experimental uncertainties, each XMCD presented here is the average of up to 16 spectra for each helicity, obtained by switching the light polarization.

Ru L_3 HERFD-XANES measurements were recorded using the in-vacuum TEXS spectrometer at the ID26 beamline[17] of the European Synchrotron Radiation Facility (ESRF) in Grenoble, France. The incident energy was tuned across the Ru L_3 edge by means of a pair of cryogenically cooled Si (111) crystals. The Ru L_3 HERFD-XANES measurements were recorded by monitoring the intensity at the top of the $L_{\alpha 1}$ emission line ($3d_{5/2} \rightarrow 2p_{3/2}$ transition) using five Si (111) crystal analyzers. The overall energy broadening was estimated to be 1.3 eV, calculated using the algorithm proposed in ref 18 assuming the Si(111) monochromator resolution to be 0.4 eV at 2.84 keV and the emission spectrometer energy bandwidth to be 1.2 eV; the widths of the L_3 (2.0 eV) and M_5 (0.24 eV) levels were taken from ref 19. We note that HERFD-XANES measurements reported in this paper were collected on concentrated pellets of the sample mixed with cellulose, and they were not corrected for self-absorption effects that can alter the relative intensities of the spectral features with respect to those recorded in conventional TEY and transmission modes. Besides the spectral resolution, the main gain of the HERFD detection mode here relies on the improved detection limit by minimizing the background signal,[14] so it is especially suitable for recording the XANES spectra at the Ru $L_{2,3}$ edges for low concentrated samples. HERFD-XANES spectra shown here have been normalized to unity at high energy, about 20 eV above the absorption edge.

Mn and Ru K-edge XANES and EXAFS measurements were performed at the BM23 beamline[20] at ESRF in Grenoble, France. Spectra were collected in transmission geometry by using ionization chambers as detectors. Manganese foil and metallic ruthenium were measured simultaneously with the samples using the third ionization chamber for energy calibration. The EXAFS data processing and analysis were performed using Demeter software.[21]

All of the XANES spectra shown here have been normalized to unity at high energy, about 40 eV above the absorption edge, after subtracting the pre-edge line.

RESULTS

Mn and Ru Magnetic Moments. Figure 1a,b presents the TEY-detected Mn $L_{2,3}$ XANES and XMCD spectra for the $Ca_3Mn_{2-x}Ru_xO_7$ ($0.05 \leq x \leq 0.9$) series at 50 K after field cooling under an applied magnetic field of 6 T. The spin-averaged XANES signals are quite similar for all Ru substitutions, indicating small variations in the electronic state of Mn atoms. The spectral shape closely resembles that of $CaMnO_3$,[22] with a dominant feature at 642.3 eV and a very narrow low-energy shoulder at 640 eV, in agreement with an average Mn oxidation state close to +4 in $Ca_3Mn_{2-x}Ru_xO_7$ for most Ru contents. A slight shift of the main peak to lower energy is observed only for very large Ru concentrations ($x \geq 0.7$). In contrast, a large difference in the magnitudes of the Mn $L_{2,3}$ XMCD signals for the different Ru substitutions is observed in Figure 1b. The XMCD signal amounts to about 2.5−2.75% of the spin-average XANES maximum at the Mn L_3 edge for the highest concentrations of Ru ($x \geq 0.7$) and to about 0.4−0.5% for the lowest Ru contents ($x \leq 0.1$).

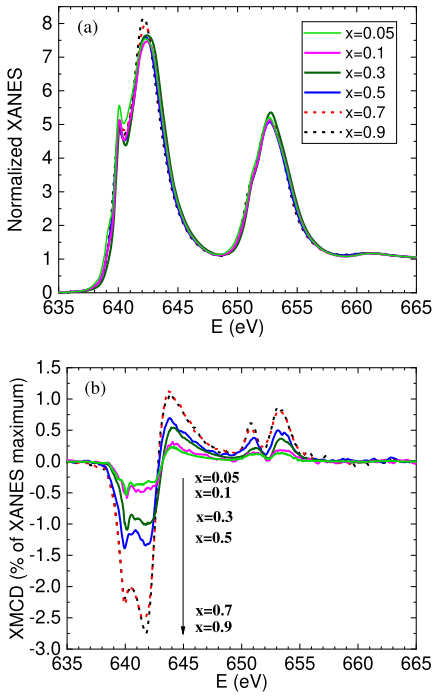

Figure 1. Normalized TEY-detected Mn $L_{2,3}$ XANES (a) and XMCD (b) spectra measured at 6 T and T = 50 K of $Ca_3Mn_{2-x}Ru_xO_7$ samples for different Ru contents (x).

Figure 2 presents the Ru L_3 and L_2 TEY-detected XAS and XMCD spectra of the $Ca_3Mn_{2-x}Ru_xO_7$ ($0.3 \leq x \leq 0.9$) series at 50 K after field cooling under an applied magnetic field of 6 T. The strong Ru 2p spin−orbit coupling heavily splits the spectrum into two well-separated spectral regions, with the Ru L_3 absorption edge falling at $E \approx 2845$ eV (Figure 2a) and the Ru L_2 at $E \approx 2973$ eV (Figure 2b). We observe very weak Ru $L_{2,3}$ XMCD signals, which are of opposite sign to those measured at the Mn $L_{2,3}$ edges (Figure 1b). This indicates that the small net Ru 4d magnetic moment is antiferromagnetically coupled to the net Mn 3d magnetic moment. In this case, the XMCD signal is about 0.3% of the spin-average XANES maximum at the Ru L_3 edge for all Ru concentrations ($x \geq 0.3$).

In order to obtain quantitative magnetic moments for the Mn and Ru atoms, we applied the so-called sum rules to the experimental XMCD spectra. Thus, the expectation values of the z component of the atomic operators $\langle SE_Z \rangle$ (effective spin), $\langle S_Z \rangle$ (spin), $\langle L_Z \rangle$ (orbital), and $\langle T_Z \rangle$ (magnetic dipole) were obtained from the following expressions:[23,24]

$$2\langle SE_z \rangle = 2\left(\langle S_z \rangle + \frac{7}{2}\langle T_z \rangle\right) = \frac{6p - 4q}{r} n_h$$

https://doi.org/10.1021/acsomega.4c04334
ACS Omega 2024, 9, 41396−41407

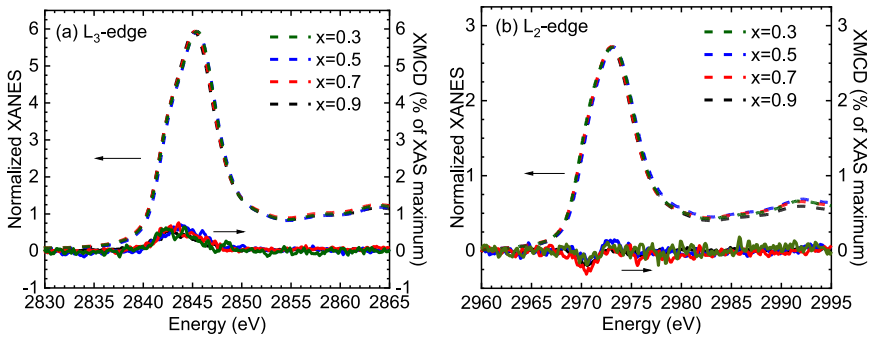

Figure 2. Normalized TEY-detected XANES (dashed lines) and XMCD (solid lines) spectra at the Ru L_3 (a) and L_2 (b) absorption edges for Ru substitutions $x \geq 0.3$ under an applied external field of 6 T and T = 50 K.

Table 1. Projection of Effective Spin (m_{SE}), Spin (m_S), Orbital (m_L), and Total (m_T) Magnetic Moments Per Mn and Ru Atoms Along the Field Direction at 50 K and 6 T as Obtained From the XMCD Spectra in the $Ca_3Mn_{2-x}Ru_xO_7$ Series[a,b]

	$Ca_3Mn_{2-x}Ru_xO_7$ sample	x = 0.05	x = 0.1	x = 0.3	x = 0.5	x = 0.7	x = 0.9
Mn	m_S (μ_B/Mn)	0.042(2)	0.046(6)	0.094(1)	0.136(7)	0.226(4)	0.234(2)
	m_L (μ_B/Mn)	0.004(1)	0.003(2)	0.011(1)	0.008(4)	0.024(3)	0.025(6)
	m_L/m_S	0.095(19)	0.065(68)	0.117(10)	0.059(37)	0.106(14)	0.107(24)
	m_T (μ_B/Mn)	0.054(4)	0.058(8)	0.124(2)	0.171(11)	0.295(7)	0.306(8)
Ru	m_{SE} (μ_B/Ru)	-	-	−0.009(9)	−0.019(8)	−0.035(15)	−0.019(6)
	m_L (μ_B/Ru)	-	-	−0.012(5)	−0.022(2)	−0.013(1)	−0.018(3)
	m_L/m_{SE}	-	-	1.333(19)	1.158(6)	0.371(2)	0.947(5)
	m_T (μ_B/Ru)	-	-	−0.021(14)	−0.041(10)	−0.048(16)	−0.037(9)
	M_{XMCD} (μ_B/f.u)	0.109(8)	0.110(13)	0.204(4)	0.236(14)	0.350(15)	0.303(9)
	M_{SQUID} (μ_B/f.u)	-	0.095	0.125	0.16	0.205	0.215

[a]The total magnetization deduced from the XMCD (M_{XMCD}) has been obtained using the Mn and Ru and the B-atom concentration. [b]The total magnetization deduced from the SQUID measurements (M_{SQUID}) has been determined from the M−H curves at 50 K and extrapolated up to 6 T.

$$\langle L_z \rangle = \frac{4q}{3r} n_h$$

where n_h is the number of holes in the Mn 3d shell (nominally, 7 for Mn^{4+}) or the Ru 4d shell (nominally, 6 for Ru^{4+}), r is the integrated area of the isotropic XANES spectrum (obtained as the sum of the recorded XANES spectra with plus and minus photon helicities) over the $L_{2,3}$ edges, and q and p are the values of the integrated areas of the XMCD signal beyond the Mn (Ru) $L_{2,3}$ signals and in between the Mn (Ru) L_3 and L_2 signals, respectively. The spin sum rule gives the expectation value of the effective spin $\langle SE_z \rangle = \langle S_z \rangle + \frac{7}{2}\langle T_z \rangle$, so an estimation of $<T_Z>$ is needed in order to determine $<S_Z>$. The contribution of $<T_Z>$ can be neglected as compared to $<S_Z>$ for the Mn^{4+} ions in an octahedral environment.[25] In this case, the orbital and spin magnetic moments are related to the above expectation values of the atomic operators through the relations: $m_L = -<L_Z>$ and $m_{SE} = -2 <SE_Z> \sim m_s = -2 <S_Z>$ in units of μ_B/atom, respectively. It is well-known that the 2p spin−orbit splitting of Mn ions is not large enough to obtain accurate $<S_Z>$ values from the spin sum rule (they tend to be largely underestimated). Thus, the Mn spin magnetic moment m_s needs to be multiplied by a correction factor that deals with the mixing of the L_3 and L_2 edges. Several correction factors ranging from 1.2 up to 1.7 have been used in the literature for the Mn spin moment.[25−27] Guo et al.[26] used a correction factor of 1.2 for the closely related ordered double perovskite La_2NiMnO_6 with Mn in a Mn^{4+} oxidation state, similar to the present case. Therefore, a correction factor of 1.2 is a reasonable estimate. By applying this correction factor, we obtained total magnetic moments that closely match the values derived from the SQUID measurements. On the other hand, the $<L_Z>$ values are far more accurate since they are directly related to the total XMCD integral. Therefore, we estimated the total magnetic moment of Mn for each composition as $m_T = 1.2m_s + m_L$. The m_s, m_L, and m_T values and the ratio (m_L/m_S) thus obtained from the aforementioned equations for the Mn atom are shown in Table 1. The Mn $L_{2,3}$ XMCD signal is dominated by the spin component and the orbital angular moment is essentially quenched (∼1/10 of the spin moment), as expected for the $3d^3$ ($t_{2g\uparrow}^3$) Mn^{4+} electronic configuration since the majority t_{2g} shell is fully occupied, leaving no orbital degrees of freedom.

The results of the application of sum rules to the experimental Ru $L_{2,3}$ XMCD spectra are also reported in Table 1. We can see that negative values are found for the Ru 4d magnetic moments in all samples, within the error bar, and spin and orbital magnetic moments are parallel in the configuration $(t_{2g})^4$ appropriate for Ru^{4+} in a strong octahedral ligand field. We note that in this case, the value of m_{SE} obtained from the spin sum rule does not require any correction factor, so $m_T = m_{SE} + m_L$. We also find a relatively large orbital to spin moment ratio, which agrees with a relevant orbital moment, which supports the existence of strong spin−orbit coupling effects. This observation is in agreement with previous investigations in the end-member $Ca_3Ru_2O_7$ compound.[28]

The derived Mn and Ru magnetic moments indicate that the Mn magnetic sublattice dominates the total magnetization since the values are about 1 order of magnitude larger than those for Ru. The positive (negative) signs of Mn (Ru) magnetic moments show that the net Mn (Ru) moments are parallel (antiparallel) to the applied magnetic field. The small

https://doi.org/10.1021/acsomega.4c04334
ACS Omega 2024, 9, 41396−41407

value of the net Ru magnetic moment, even at high Ru contents, agrees with AFM ordering of the Ru sublattice. Although the spin−orbit coupling plays a role in Ru^{4+} compounds, no Van Vleck-type temperature-independent magnetism, as expected for a $J = 0$ system, was observed in the $Ca_3Mn_{2-x}Ru_xO_7$ compounds.[13] Instead, the effective moment obtained from a Curie−Weiss fit agrees with a low spin Ru^{4+} ($S = 1$) state.

The Mn sublattice also orders antiferromagnetically for very low Ru contents ($x \leq 0.1$). Although the Mn magnetic moment increases for $x \geq 0.3$, the values are substantially lower than expected (3 μ_B) for a fully polarized Mn^{4+} magnetic sublattice according to Hund's rule. Since the Mn $L_{2,3}$ XMCD signal is related to the value of the Mn^{4+} spin projected along the direction of the applied magnetic field, these results point out an intrinsic canting of the antiferromagnetically ordered Mn^{4+} spins, which gets enhanced by Ru substitution. XMCD measurements were also conducted in remanence to delve deeper into the origin of the canted FM component with Ru substitution. Samples were first field-cooled at 6 T down to 50 K, then the field was removed and the dichroic signal was measured. The Mn $L_{2,3}$ XMCD is still visible under these conditions (about 10% of the value at 6 T) and it keeps the same sign for $x \geq 0.3$ (Figure 3), but no clear remanence signal

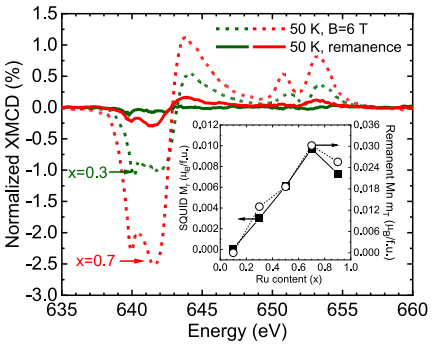

Figure 3. Experimental Mn $L_{2,3}$ XMCD spectra at 50 K under an applied magnetic field of 6 T (dashed lines) and in remanence (solid lines) for $Ca_3Mn_{2-x}Ru_xO_7$ samples with $x = 0.3$ and 0.7 Inset: remanent magnetization of the $Ca_3Mn_{2-x}Ru_xO_7$ samples with $0.1 \leq x \leq 0.9$ as measured at 50 K with SQUID (squares) compared to the total remanent Mn magnetic moment deduced from the Mn $L_{2,3}$ XMCD spectra at 50 K.

is observed for $x \leq 0.1$. The remanent XMCD signals measured at the Mn $L_{2,3}$ edges qualitatively agree with the macroscopic remanent magnetization measured using conventional magnetometry as shown in the inset of Figure 3. In conclusion, the Mn XMCD results provide additional evidence of the presence of a small intrinsic FM component measured by magnetometry, at least for Ru contents $x \geq 0.3$, which could not be detected by NPD due to sensitivity limitations of the technique, although it is noteworthy that such FM component is allowed by symmetry along the c axis.[13] Furthermore, the canting can be mainly ascribed to the Mn magnetic sublattice, but it is induced by the Ru substitution.

Mn and Ru Valence States. Normalized XANES spectra at the Mn K-edge (Figure 4a) show minimal change in the spectral shape for the $Ca_3Mn_{2-x}Ru_xO_7$ ($0 \leq x \leq 0.9$) series. Thus, Mn remains essentially 4+ as in the undoped compound. We observe a tiny shift toward lower energies, 0.6 eV for $x \geq 0.7$, indicative of a slight reduction of the Mn atoms upon

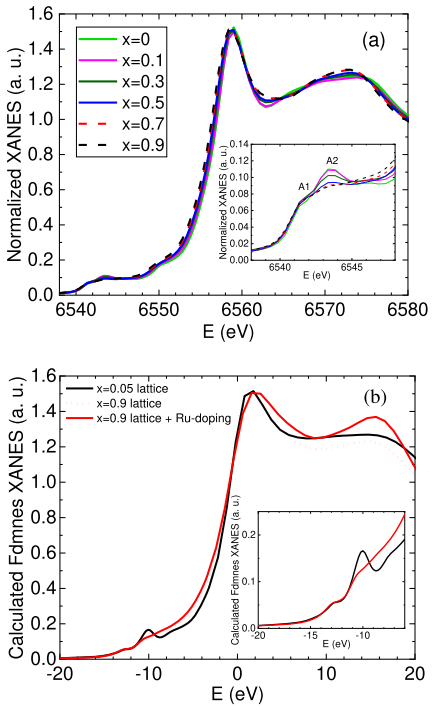

Figure 4. (a) Normalized Mn K-edge XANES spectra taken in transmission for the $Ca_3Mn_{2-x}Ru_xO_7$ ($0 \leq x \leq 0.9$) samples at room temperature. Inset: Detail of the pre-edge region . (b) Multiple scattering calculations for a cluster with $R = 6$ Å at the Mn K-edge for the $Ca_3Mn_{1.95}Ru_{0.05}O_7$ (black solid line) and $Ca_3Mn_{1.1}Ru_{0.9}O_7$ (red dashed line) samples using their corresponding crystallographic structure with 6 Mn second neighbors and for $Ca_3Mn_{1.1}Ru_{0.9}O_7$ also using its crystallographic structure but considering 3 Mn and 3 Ru as second neighbors (red solid line). The zero energy corresponds to the absorption edge energy. Inset: Detail of calculations for the pre-edge region.

increasing the Ru content. A chemical shift of 4.2 eV is observed between Mn oxides with formal Mn^{3+} and Mn^{4+} valence states.[29] Based on the empirical linear correlation between this chemical shift and the Mn formal valence state, Mn is found to be in a + 3.86 oxidation state for $x \geq 0.7$, in agreement with the results from soft X-ray TEY-detected XANES spectra at the Mn $L_{2,3}$ edges (Figure 1a). Interestingly, the XANES spectra recorded in transmission are well resolved at the pre-edge region to follow the evolution of the intensity of main feature A2 (inset of Figure 4a). The intensity of this peak A2 decreases with increasing Ru substitution, but it is drastically reduced for $x \geq 0.5$. The Mn K pre-edge peaks in manganese perovskites are mainly attributed to 1s to 4p dipole transitions. However, transitions to (i) local 3d−4p mixed states at the absorbing Mn site if this site is not centrosymmetric and (ii) nonlocal 3d/4d states of neighboring metal sites through the oxygen mediated intersite hybridization M(4p)−O(2p)−M'(3d/4d) may contribute to the intensity of these peaks.[30]

According to the present Mn K-edge XANES (Figure 4a) and our previous Mn $L_{2,3}$ soft XAS measurements (Figure 1a), Mn maintains a valence state close to 4+ along the whole series. This agrees with the fact that the pre-edge A1 feature arises from local dipole (and quadrupole) transitions to the empty 3d states of the absorbing Mn atom since it is almost unaltered with Ru substitution. As a consequence, the sudden decrease of the pre-edge A2 feature intensity has to be mostly

https://doi.org/10.1021/acsomega.4c04334
ACS Omega 2024, 9, 41396−41407

related to the metal-to-metal intersite oxygen mediated hybridization. The strength of this nonlocal dipole contribution depends on the degree of O covalence, i.e. the M−O bond lengths and the M−O−M′ bond angles that regulate the orbital overlap. NPD measurements in $Ca_3Mn_{2-x}Ru_xO_7$[13] have shown that the tilts of the MO_6 octahedra are larger with increasing Ru content, to relieve the structural strain. This results in a decrease of the M−O−M' bond angles, which is accompanied by the appearance of a tensile stress on the MnO_6 octahedra. The combination of these two steric effects favors a reduction of the intersite hybridization. Furthermore, for the highest Ru contents, Mn is surrounded by almost an equal number of Ru and Mn neighbors and the strong reduction of the intersite hybridization could be also enhanced by the incorporation of Ru as Ru^{4+} low spin with less empty t_{2g} orbitals than Mn^{4+}.

In order to clarify the origin of the pre-edge A2 feature, we have performed multiple scattering theoretical calculations of the XANES spectra using the FDMNES code (version February 2016)[31] under the Green formalism in the muffin-tin approach. The cluster geometry was fixed to the structural determination by NPD for each Ru x concentration.[13] Figure 4b shows the 6 Å radius cluster calculations, where the black solid and red dashed lines represent the crystal lattices of the x = 0.05 and 0.9 samples, respectively, considering only Mn atoms as neighbors of the Mn absorber. The calculation using the same crystallographic structure of the x = 0.9 sample but considering the effect of Ru substitution (3 Ru neighbors on the first shell of the Mn atom) corresponds to the red solid line. The agreement with the experimental measurements presented in Figure 4a is reasonably good in regards to the main edge energy shift and the structure that appears at about 15 eV above the edge. Regarding the pre-edge A2 peak (inset of Figure 4b), it is clear that its intensity is not modified much by the structural changes due to the Ru incorporation (red dashed line in the calculations). On the contrary, it is very sensitive to the presence of Ru neighbors around the absorbing Mn atom (red solid line in the calculations). This confirms that the peak A2 originates from nonlocal dipole 1s → p transitions, where the empty p states of the absorbing Mn atom are hybridized with the 3d and 4d states of the second Mn and Ru neighbors (in a ratio 3:3 for x = 0.9). This is in line with Mn primarily surrounded by low spin Ru^{4+} (t_{2g}^4), given that the hybridization in that scenario is reduced in comparison to the case when the absorbing Mn is completely surrounded by 6 Mn^{4+} (t_{2g}^3).

The spectral line shape of normalized XANES spectra at the Ru K-edge (Figure 5) also shows minimal changes for the $Ca_3Mn_{2-x}Ru_xO_7$ ($0.3 \le x \le 0.9$) series. The reported chemical shift between Ru^{4+} and Ru^{5+} oxides at the Ru K-edge is around 2 eV.[32] Here, a chemical shift of ∼0.9 eV to higher energies is observed between the $x \ge 0.7$ compounds and a Ru^{4+} reference (La_2ZnRuO_6 sample), which means that Ru is in an intermediate valence state of ∼$Ru^{4.4+}$ for these compositions. With decreasing the Ru content down to x = 0.3, a shift of about 0.4 eV to higher energies is found (see the inset of Figure 5), which agrees with a $Ru^{4.6+}$ for the x = 0.3 compound. Therefore, the Ru valence state remains intermediate for all the Ru concentrations but slightly approaches the Ru^{4+} oxidation state as the Ru content increases.

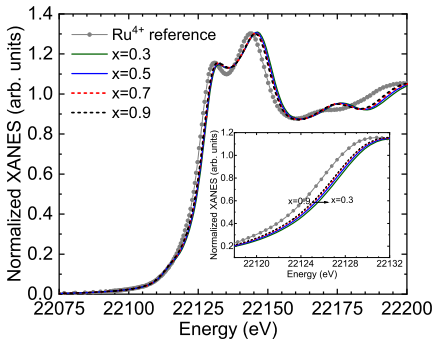

Figure 5. Room temperature normalized Ru K-edge XANES spectra taken in transmission for the $Ca_3Mn_{2-x}Ru_xO_7$ ($0.3 \le x \le 0.9$) samples compared with La_2ZnRuO_6 as the reference for Ru^{4+}. Inset: detail of the edge region showing the tiny chemical shift with decreasing Ru content.

In order to cover the whole $Ca_3Mn_{2-x}Ru_xO_7$ ($0.05 \le x \le 0.9$) series, we also examine the Ru valence states through the Ru L_3 XANES spectra measured by HERFD and TEY-detection modes. Figure 6 compares the XANES spectra of the

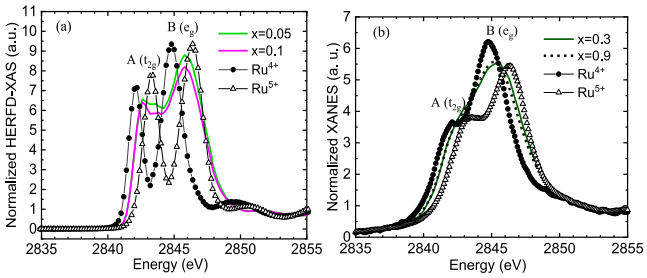

Figure 6. (a) Comparison between the room temperature normalized HERFD-XANES spectra taken at the maximum of Ru $L_{\alpha 1}$ emission line for low-doped $Ca_3Mn_{2-x}Ru_xO_7$ ($x \le 0.1$) samples and the La_2ZnRuO_6 (Ru^{4+}) and Ba_2YRuO_6 (Ru^{5+}) references. (b) Normalized Ru L_3 TEY-detected XANES spectra for selected $Ca_3Mn_{2-x}Ru_xO_7$ (x = 0.3, 0.9) samples compared to the La_2ZnRuO_6 (Ru^{4+}) and Ba_2YRuO_6 (Ru^{5+}) references at room temperature.

$Ca_3Mn_{2-x}Ru_xO_7$ ($0.05 \le x \le 0.9$) series to those of La_2ZnRuO_6 and Ba_2YRuO_6 reference compounds. We note that, in the low doping regime ($x \le 0.1$), spectra could only be measured in the HERFD-detection mode, profiting from its inherent improved signal-to-noise ratio, almost background-free, over standard X-ray absorption spectroscopy detection modes. Thus, it is ideal in the case of low elemental concentrations.[14] However, being a fluorescence-detection-based method, HERFD is prone to self-absorption effects. HERFD-XANES spectra of the whole $Ca_3Mn_{2-x}Ru_xO_7$ ($0.05 \le x \le 0.9$) series are displayed in Figure S1, where looking at the relative intensity of the observed spectral features, it is clear that self-absorption effects are important on samples with $x \ge 0.3$ as Ru is then less and less diluted on the matrix. Therefore, we restrict the evaluation of the Ru valence state through HERFD-XANES to the lowest Ru content samples (x = 0.05, 0.1).

The Ru L_3-edge HERFD-XANES spectra of both references exhibit a well-resolved doublet with two peaks (A and B) ascribed to dipolar transitions from Ru 2p states to 4d states, the latter being split by the crystal field with octahedral symmetry into t_{2g} and e_g levels separated by $\Delta = 10D_q$. The peak energy positions (E_A and E_B) shift to higher energies for

https://doi.org/10.1021/acsomega.4c04334
ACS Omega 2024, 9, 41396−41407

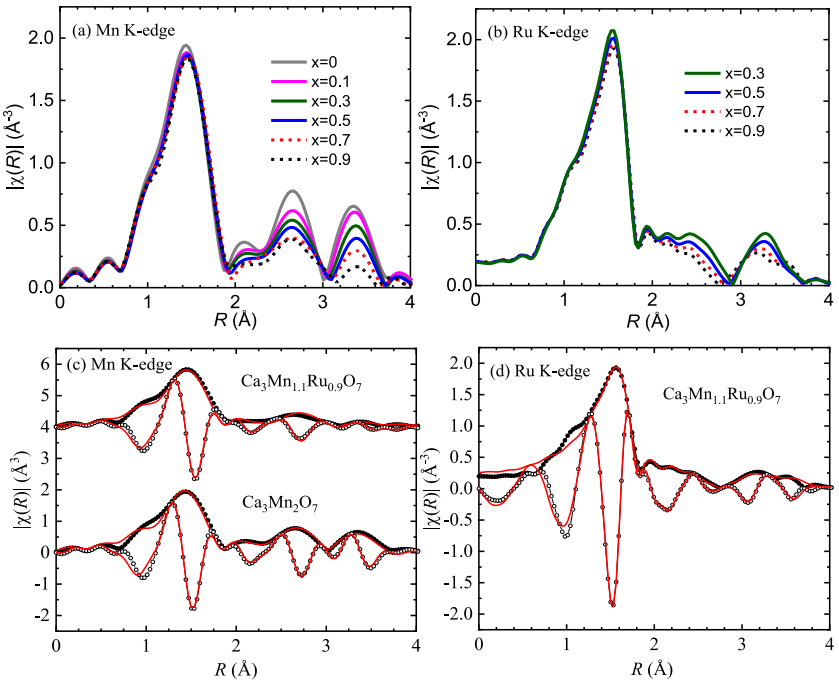

Figure 7. Magnitude of Fourier transform of k^2-weighted EXAFS oscillations for $Ca_3Mn_{2-x}Ru_xO_7$ samples at the Mn K-edge (a) and Ru K-edge (b). The $|\chi(R)|$ plots are not corrected for phase shifts. Magnitude and imaginary parts of the k^2-weighted EXAFS oscillations (close and open circles, respectively) along with best fitting results (lines) at Mn K-edge (c) and Ru K-edge (d) of $Ca_3Mn_{2-x}Ru_xO_7$ (x = 0 and 0.9) samples. See Table 2 for refined structural parameters obtained from the analysis.

Ba_2YRuO_6 according to the higher oxidation state of the Ru ion (formal Ru^{5+}) in this sample. The energy shifts of the A and B peaks between these reference samples are about 1.2 ± 0.1 and 1.6 ± 0.1 eV, respectively, in agreement with the chemical shift of about 1.5 eV[33,34] previously reported from Ru^{4+} to Ru^{5+}. Ru oxidation is further evidenced from the analysis of the t_{2g}/e_g peak ratio and $t_{2g}-e_g$ energy splitting (ΔE). Greater energy splitting ΔE in Ru L_3-edge XAS spectra comes from larger ligand fields associated with higher oxidation states and removal of 1 e^- from Ru^{4+} is accompanied by a larger ratio of the integrated area of the t_{2g} peak and e_g peak. The ratios between both peak areas from HERFD-XANES for the reference samples are At_{2g}/Ae_g = 0.5 (Ru^{4+}) and 0.66 (Ru^{5+}). The expected values are 0.5 (Ru^{4+} low spin) and 0.75 (Ru^{5+}) considering ($t_{2g}^4e_g^0$) and ($t_{2g}^3e_g^0$) electronic configurations for Ru^{4+} low spin and Ru^{5+}, respectively. The experimental ratio is coincident with the theoretical one for the Ru^{4+} reference while it is slightly smaller in the case of the Ru^{5+} reference. This effect might indicate that Ru^{5+} is better described by a combination of Ru^{5+} and $Ru^{4+}L$ where L denotes a ligand hole at the oxygen position. On the other hand, the energy splitting ΔE increases from 2.7 eV in La_2ZnRuO_6 to 3 eV in Ba_2YRuO_6, in agreement with the higher Ru oxidation in the latter.

The Ru L_3 HERFD-XANES of the low-doped $Ca_3Mn_{2-x}Ru_xO_7$ ($x \leq 0.1$) samples is shifted to higher energies with respect to the formal Ru^{4+} reference by about 1 eV (see Figure 6a). Assuming a linear dependence of the chemical shift on the formal oxidation state of the absorbing species, Ru would agree with the +4.7 oxidation state in the $Ca_3Mn_{2-x}Ru_xO_7$ ($x \leq 0.1$) samples. Besides, the energy splitting between t_{2g} and e_g features (ΔE) is found to be 3.2 eV, closer to the value correspondent to a Ru^{5+} oxidation state. On the other hand, the spectral line shapes of these low-doped compounds reveal changes in the width and asymmetry of the two white line peaks A and B that are not observed in the reference ones. In particular, they result in a broadening of the peak B (e_g) and the appearance of an additional feature between the peak A (t_{2g}) and B (e_g). This complex shape of the white line peaks has been ascribed to a distorted octahedral environment around Mo atoms in a recent Mo L_3 HERFD-XANES study in a series of Mo compounds with similar crystal-field-split unoccupied 4d states as in our Ru-doped HIF systems.[35]

For $x \geq 0.3$, the Ru L_3-edge HERFD-XANES spectra, reported in Figure S1, are found to be slightly shifted back to a lower photon energy, indicating a slight Ru reduction, in agreement with the results obtained from the analysis of the Ru K-edge XANES measurements. Quantification of the Ru oxidation state using ΔE shows similar reduction trends from 3 eV down to 2.7 eV, typical of a Ru^{4+}. Figure 6b reports the Ru L_3 TEY-detected XANES spectra for the medium (x = 0.3) and high (x = 0.9) Ru contents. In this case, the low-energy peak A (t_{2g} states) is not clearly distinguishable, but the maximum of peak B (e_g states) is slightly shifted to higher energies with respect to the formal Ru^{4+} reference. Thus, following the relationship between energy shift and oxidation state, we infer that $Ru^{4.5+}$ and $Ru^{4.4+}$ intermediate states would be present in the $Ca_3Mn_{1.7}Ru_{0.3}O_7$ and $Ca_3Mn_{1.1}Ru_{0.9}O_7$ samples, respectively, according to the observed shift. This finding is consistent with the valence states deduced for the Ru atom from the Ru K-edge XANES analysis within an error of ±0.1.

In summary, according to our combined soft and hard X-ray spectroscopic study, Ru incorporates into $Ca_3Mn_2O_7$ at low doping levels ($x \leq 0.1$) as a $Ru^{4.7+}$ intermediate valence state and shows a continuous reduction down to $Ru^{4.4+}$ in $Ca_3Mn_{1.1}Ru_{0.9}O_7$. Instead, Mn remains essentially 4+ along

https://doi.org/10.1021/acsomega.4c04334
ACS Omega 2024, 9, 41396−41407

the whole series, although a slightly reduced $Mn^{3.85+}$ is also obtained at $x \geq 0.7$. The observed gradual decrease of the nominal valence states of Ru and Mn atoms with the Ru content was found previously in the $CaRu_{1-x}Mn_xO_3$ series[36] for $x \geq 0.55$. These results demonstrate the complexity of the electronic structure of these Mn−Ru mixed valence oxides, which does not result from simply replacing two Mn^{4+} by Ru^{5+} and Mn^{3+}. On the other hand, the intermediate valence state of the Ru atoms in these HIF systems is likely due to local structural steric effects and the most plausible scenario is as follows. When incorporating a small amount of Ru into the $Ca_3Mn_2O_7$ matrix, Ru−O bonds are too short, and Ru is strongly overbonded. To accommodate at the Mn^{4+} site, provided by the stronger hybridization of the Ru 4d states with the oxygen 2p ones compared to Mn 3d states, charge transfer between Ru and neighboring oxygen atoms takes place and results in a higher oxidation state $Ru^{4.7+}$ (while Mn remains +4). Upon further increasing the Ru content, the unit cell volume increases and Ru is less overbonded, while Mn is slightly underbonded. This results in an intermediate valence state for Ru (+4.4) closer to Ru^{4+} being Mn slightly reduced to a +3.85 valence state. Although charge transfer between Ru (and also Mn for $x \geq 0.7$) and O atoms seems the most plausible mechanism (formal valence for oxygen atoms would slightly change between −2.01 and −2.03 throughout the series), the existence of interstitial sites for oxygen atoms in the rock-salt Ca−O layer prevents ruling out the role of an oxygen excess.

Mn and Ru Local Structure. Structural information on the local environment of the Mn and Ru atoms along the $Ca_3Mn_{2-x}Ru_xO_7$ ($0.3 \leq x \leq 0.9$) series was extracted from their respective Mn and Ru K-edge EXAFS spectra. Experimental EXAFS data acquired up to 14 $Å^{-1}$ and 20 $Å^{-1}$ in k space for Mn and Ru K-edges, respectively, are shown in Figure S2a,b. The magnitudes of the Fourier transforms (FTs) of the k^2-weighted EXAFS oscillations are plotted in Figure 7a,b, in the k range between 2 and 12.5 $Å^{-1}$ and 3 and 18.5 $Å^{-1}$ for Mn and Ru K-edges, respectively. Both Mn K-edge and Ru K-edge EXAFS signals plotted in R space show three peaks: the first one corresponds to the Mn(Ru)O_6 octahedron (first coordination shell), while the next two peaks come from the scattering from its Ca (∼2.65 Å) and Mn/Ru (∼3.4 Å) neighbors, respectively (second coordination shell). The substitution of Mn with Ru leads to insignificant changes in the Mn−O environment in the first shell. In contrast, the Mn−Ca and Mn−Mn(Ru) coordination peaks significantly decrease as the Ru content increases (Figure 7a). On the other hand, the inspection of the first peak of the FT of the Ru K-edge EXAFS signals (Figure 7b) discloses a slight reduction of the Ru−O coordination in intensity accompanied by a tiny increase of the bond distance with doping. Similar to the Mn K-edge results, a decrease of the Ru−Ca and Ru−Mn(Ru) coordination with Ru content is also found.

The analysis of the EXAFS signals was conducted considering only single-scattering paths in the first step, in order to unveil the local atomic arrangement around Mn and Ru, and to provide evidence for the eventual formation of a solid solution at the atomic scale. Multiple-scattering paths were considered only to evaluate the quality of the fit. In general, the inclusion of multiple scattering paths does not lead to a significant improvement in the accuracy of structural information. Fits were then made considering Mn(Ru)−O, Mn(Ru)−Ca and Mn(Ru)−Mn(Ru) coordination shells, covering the range up to 4 Å. The substitution of manganese for ruthenium was achieved by using the crystal structure of either $Ca_3Mn_2O_7$ or $Ca_3Mn_{1.1}Ru_{0.9}O_7$. In this way, FEFF calculations[37] were used to fit the signals, identified as follows: (1) Mn−$Ca_3Mn_2O_7$, (2) Mn−$Ca_3Mn_{1.1}Ru_{0.9}O_7$, (3) Ru−$Ca_3Mn_{1.1}Ru_{0.9}O_7$, and (4) Ru−$Ca_3Mn_2O_7$, where the first element represents the absorber (Mn for (1) and (2) or Ru for (3) and (4)), and the rest of the paths were calculated upon the corresponding crystal structure ($Ca_3Mn_2O_7$ or $Ca_3Mn_{1.1}Ru_{0.9}O_7$), considering that the Mn sublattice is randomly substituted by Ru at the B site, in line with the appropriate chemical composition. The resulting pathway amplitudes were multiplied by the occupancy for the element involved.

Figure 7 also shows the fits to the EXAFS signals of the end-member materials $Ca_3Mn_2O_7$ (at the Mn K-edge) and $Ca_3Mn_{1.1}Ru_{0.9}O_7$ (at both Mn and Ru K-edges) as an example, with the derived structural parameters, namely, bond lengths and Debye−Waller (DW) factors, provided in Table 2. Similar analysis of the $Ca_3Mn_{2-x}Ru_xO_7$ ($0.1 \leq x \leq 0.7$) samples is presented in the Supporting Information. The Mn K-edge EXAFS signals can be satisfactorily fitted with the structural model (1) Mn−$Ca_3Mn_2O_7$ for the lower Ru contents $x \leq 0.5$ where the contribution of the second Ru shell to the EXAFS is negligible. For $x \geq 0.7$, the structural parameters for the first O shell and second Ca and Mn shells agree with the FEFF calculation (1) Mn−$Ca_3Mn_2O_7$ as for the lower Ru content, but the best fit for the Mn−Ru path is consistent with that of the crystal structure of $Ca_3Mn_{1.1}Ru_{0.9}O_7$ (FEFF calculation (2)). The Mn−O bond distance along the $Ca_3Mn_{2-x}Ru_xO_7$ ($0 \leq x \leq 0.9$) series ranges between 1.883(4) and 1.906(4) Å. These values are barely dependent on the Ru content and agree well with the value expected for a Mn^{4+}−O bond length.[38] Furthermore, the first shell peak intensities and consequently the DW factors of the Mn−O bond distance remain nearly unchanged within the error (∼0.0020(6) $Å^2$, Tables 2 and S1), which indicates the stability of a regular oxygen environment around the Mn atom upon Ru substitution. The position of the two peaks corresponding to the Mn−Ca and Mn−Mn(Ru) distances does not significantly change with Ru content, as expected for a stable cation arrangement around the Mn atom. The intensities of these two peaks, however, decrease with increasing Ru concentration, especially for the Mn−Mn(Ru) distance at approximately 3.4 Å. This behavior agrees with an increase of the DW factors for these paths, as expected for an enhanced structural disorder as Mn is diluted with Ru, extending in the material beyond the first oxygen coordination shell.

On the other hand, the Ru K-edge EXAFS signals are satisfactorily fitted with the structural model (3) Ru−$Ca_3Mn_{1.1}Ru_{0.9}O_7$ for all the Ru contents. The Ru−O bond distance along the $Ca_3Mn_{2-x}Ru_xO_7$ ($0.3 \leq x \leq 0.9$) series ranges between 1.958(2) and 1.974(2) Å. These values slightly increase with increasing Ru content, but they are clearly smaller than the Ru−O bond length for the Ru^{4+} reference La_2ZnRuO_6 sample (R_{Ru-O} = 2.001(2) Å; σ^2= 0.0031(2) $Å^2$). This value perfectly agrees with previous EXAFS analysis in the La_2ZnRuO_6 sample that estimates a Ru^{4+}−O distance of 1.996 Å.[33] In this work, they report on a Ru^{5+}−O distance of 1.953 Å in Ba_2YRuO_6, very similar to the value obtained for the x = 0.3 sample (see Supporting Information). Furthermore, the Ru−O distances obtained from the EXAFS analysis agree with the evolution of the intermediate valence oxidation state for Ru

https://doi.org/10.1021/acsomega.4c04334
ACS Omega 2024, 9, 41396−41407

Table 2. EXAFS-Derived Parameters for $Ca_3Mn_2O_7$ at the Mn K-Edge and $Ca_3Mn_{1.1}Ru_{0.9}O_7$ at Both Mn and Ru K-Edges Obtained by Fitting the k^2-Weighted EXAFS Oscillations in *R* Space with *R*-Factors = 0.018, 0.023, and 0.008, Respectively[ab]

Path	*N*	R/Å	σ^2/Å^2
$Ca_3Mn_2O_7$ Mn K-edge			
Mn−O	6	1.883(4)	0.0018(5)
Mn−Ca	1	3.037(8)	0.0030(11)
	2	3.116(8)	0.0030(11)
	2	3.183(8)	0.0030(11)
	2	3.224(8)	0.0030(11)
	1	3.264(8)	0.0030(11)
Mn−Mn	4	3.727(13)	0.0110(19)
	1	3.816(13)	0.0110(19)
$Ca_3Mn_{1.1}Ru_{0.9}O_7$ Mn K-edge			
Mn−O	6	1.906(4)	0.0023(6)
Mn−Ca	1	3.048(13)	0.0101(21)
	2	3.128(13)	0.0101(21)
	2	3.194(13)	0.0101(21)
	2	3.235(13)	0.0101(21)
	1	3.275(13)	0.0101(21)
Mn−Mn	2.2	3.805(35)	0.0149(53)
Mn−Ru	1.8	3.866(14)	0.0078(22)
Mn−Mn	0.55	3.894(35)	0.0149(53)
Mn−Ru	0.45	3.926(14)	0.0078(22)
$Ca_3Mn_{1.1}Ru_{0.9}O_7$ Ru K-edge			
Ru−O	6	1.974(2)	0.0031(2)
Ru−Ca	1	3.074(13)	0.0090(19)
	2	3.169(13)	0.0090(19)
	1	3.218(13)	0.0090(19)
	3	3.326(13)	0.0090(19)
	1	3.493(13)	0.0090(19)
Ru−Mn	2.2	3.866(14)	0.0078(22)
Ru−Ru	1.8	3.857(25)	0.0091(33)
Ru−Mn	0.55	3.926(14)	0.0078(22)
Ru−Ru	0.45	3.917(25)	0.0091(33)

[a]The amplitude reduction factor (S_0^2) was fixed to 0.625, the value obtained for the $Ca_3Mn_2O_7$ compound, and the threshold energy (ΔE_0) was fixed to the average value of −4.33 eV (−3.52 eV) for the Mn K-edge (Ru K-edge), respectively. [b]The shell occupation numbers (*N*) were kept constant according to the chemical formula. Only, the radial distances and the DW factors were considered as fitting parameters.

atoms obtained from our XANES analysis. The RuO_6 octahedron also shows a minor distortion upon increasing the Ru content (thereby, similar DW factors, ∼0.0030(2) Å^2 within the error, see detailed fitting results in Tables 2 and S1). The refinement of the local structure of the second coordination shells around the Ru atom can be interpreted in terms of Ru substitution into the Mn site of the $Ca_3Mn_{1.1}Ru_{0.9}O_7$ lattice, but with an increased structural disorder upon increasing the Ru content similar to the Mn K-edge results.

The trend in the M−O and M−M bond length distances (*M* = Mn and Ru) with the Ru content, plotted in Figure 8 can provide us with the most evident diagnosis for the formation of a solid solution at the atomic scale. The Ru−O distances determined by EXAFS slightly increase in the $Ca_3Mn_{1.1}Ru_{0.9}O_7$-type structure with the Ru content whereas the Mn−O bond length distances remain close to the value

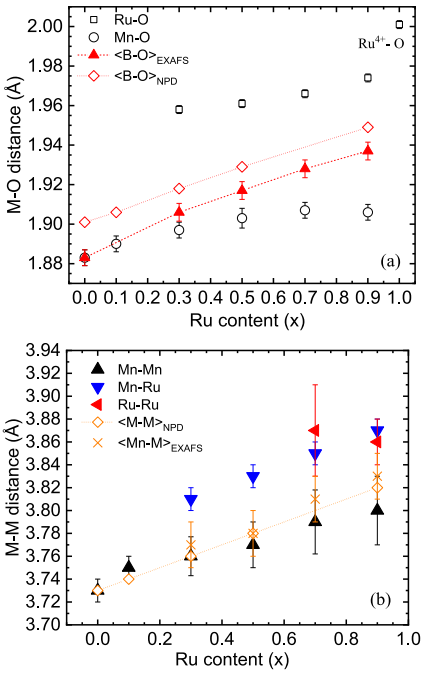

Figure 8. (a) Interatomic distances Mn−O (open black circles) and Ru−O (open black squares) vs composition in the $Ca_3Mn_{2-x}Ru_xO_7$ series. The triangle and diamond symbols represent the average values obtained from EXAFS and NPD, respectively. (b) Interatomic distances Mn−Mn (black triangles), Mn−Ru (blue triangles), and Ru−Ru (red triangles) vs composition in the $Ca_3Mn_{2-x}Ru_xO_7$ series. The cross and diamond symbols represent the average values obtained from EXAFS and NPD, respectively.

determined in the parent $Ca_3Mn_2O_7$ compound. From these results, the MnO_6 octahedron is preserved as in the host $Ca_3Mn_2O_7$ structure as Ru content increases whereas the RuO_6 octahedron is slightly modified in line with the small change derived for the average Ru oxidation state. Besides, the average EXAFS M−O distance plotted in Figure 8a shows a similar trend compared to the neutron diffraction results, although it is smaller in absolute value. This result agrees with the expected unit cell expansion with Ru substitution. The variation in the cation−cation distribution is also presented in Figure 8b. First, the Mn−Mn distances are approximately equal to their average distances but suffer a small variation from 3.75(1) to 3.80(3) Å with the Ru content, remaining close to that of $Ca_3Mn_2O_7$. On the other hand, the Mn−Ru distances are bigger than their average distances. In addition, for high Ru contents, they are similar to the Ru−Ru distances, and as the Ru content decreases, they approach the Mn−Mn ones. These results again support that even though the Ru electronic and local structure is modified, MnO_6 units are robust and remain close to that of the undoped $Ca_3Mn_2O_7$ compound.

DISCUSSION AND CONCLUSIONS

The investigation of the local electronic structure and magnetic moments of the magnetic cations in doped HIFs is key to understanding and controlling the mechanisms for promoting ferromagnetism in these materials. For this purpose, the HIF $Ca_3Mn_2O_7$, belonging to the Ruddlesden−Popper-type structure, was investigated as a function of Ru substitution by a combination of soft and hard X-ray absorption spectroscopies. The $Ca_3Mn_{2-x}Ru_xO_7$ ($0 \le x \le 0.9$) series is single-phase and shows the same polar orthorhombic structure

https://doi.org/10.1021/acsomega.4c04334
ACS Omega 2024, 9, 41396−41407

as the undoped parent compound independent of the Ru content at room temperature. Their macroscopic magnetic properties clearly reveal that ferromagnetism is enhanced by incorporating Ru into the Mn sites. However, NPD indicates that the long-range magnetic order is mainly antiferromagnetic in all samples, though by symmetry, an undetected FM component along the c axis is allowed.[13]

In this work, we show that the distinct electronic structure of both the Mn and Ru atoms in the $Ca_3Mn_{2-x}Ru_xO_7$ system is at the origin of the enhancement of ferromagnetism. The Mn $L_{2,3}$ and Ru $L_{2,3}$ XMCD spectra show that the spin moments of Mn and Ru are aligned in antiparallel directions. The XMCD data also demonstrate that although the Mn sublattice orders antiferromagnetically, there is a small intrinsic ferromagnetic component in the Mn sublattice for sufficiently high Ru contents, $x \geq 0.3$. Furthermore, this small intrinsic Mn spin moment increases with the Ru concentration. The Ru sublattice orders antiferromagnetically with no sign of intrinsic ferromagnetic component, and the small Ru magnetic moment obtained under an applied magnetic field of 6 T does not change with Ru concentration. The combined soft and hard X-ray absorption spectroscopy results show that the Mn atoms are in the Mn^{4+} state independent of the Ru content and their local environment is very stable, remaining close to that of the undoped $Ca_3Mn_2O_7$. On the other hand, Ru atoms enter the Mn sublattice in an intermediate valence state $Ru^{4.7+}$ at low doping ($x \leq 0.1$). The coexistence of Mn^{4+} and $Ru^{4.7+}$ in this low doping regime is accounted for by the ionic radius of a formal Ru^{5+} (0.565 Å) that is quite similar to that of Mn^{4+} (0.53 Å). On the other hand, a Ru^{4+} (0.62 Å) would be strongly compressed so a charge transfer from Ru to the neighboring oxygen atoms occurs due to the strong hybridization of the Ru delocalized 4d with the O 2p states. Upon increasing the Ru content, the intermediate valence state of Ru slightly decreases down to $Ru^{4.4+}$ for Ru contents $x \geq 0.7$. The local structure around the Ru atoms agrees with that of the $Ca_3Mn_{1.1}Ru_{0.9}O_7$ structure, and it is slightly modified with the Ru content (the compressive stress tends to relax associated with the lattice expansion) consistent with the small change in the average Ru oxidation state. These results indicate that since Ru 4d electrons are more itinerant than Mn 3d electrons, which are in the localized tetravalent states, the oxygen mediated magnetic coupling between neighboring Mn and Ru atoms plays a relevant role.

We can exclude the conventional double-exchange model as a possible mechanism for ferromagnetism in $Ca_3Mn_{2-x}Ru_xO_7$. Therefore, alternative models should apply, such as the one proposed for half-metallic double perovskite systems[39] and the simple $CaMn_{1-x}Ru_xO_3$ perovskites.[40] We suggest that the induced ferromagnetic coupling in the Mn magnetic sublattice in $Ca_3Mn_{2-x}Ru_xO_7$ is due to the antiparallel coupling of the itinerant intermediate-valence state Ru 4d and the localized Mn^{4+} 3d electrons in the following way: due to the strong hybridization between the extended intermediate valence Ru 4d and O 2p orbitals, the Ru t_{2g}-up spin states are pushed up above the Fermi level while the Ru t_{2g}-down spin states are pushed down.[39] With increasing Ru concentration, the electron occupation number in the Ru t_{2g}-down spin states increases according to the reported changes in the Ru valence state from +4.7 to +4.4 while Mn remains in the half-filled Mn^{4+}. Consequently, the antiparallel spin polarization at the Ru and Mn sites is induced between Ru t_{2g}-down spin states and half-filled Mn^{4+} t_{2g}-up spin states and a ferromagnetic coupling is induced between the Mn^{4+} atoms. However, the small Mn magnetic moments derived from XCMD suggest that the induced ferromagnetic coupling results only in a canting of the antiferromagnetically ordered Mn^{4+} spins. We note here that the long-range magnetic structure of $Ca_3Mn_{2-x}Ru_xO_7$ ($x \geq 0.3$) derived from NPD[13] is antiferromagnetic A_xG_y but a FM component is allowed by symmetry along the c-axis (F_z) so it can be realized by a canting of the Mn^{4+} magnetic moments out of the ab plane. In this sense, the lack of a full ferromagnetic alignment of the Mn^{4+} spins in $Ca_3Mn_{2-x}Ru_xO_7$, differently from the behavior seen in ordered double perovskites,[41] should be related to the fact that Mn and Ru atoms are completely disordered in this HIF system.

■ ASSOCIATED CONTENT

Supporting Information

The Supporting Information is available free of charge at https://pubs.acs.org/doi/10.1021/acsomega.4c04334.

HERFD-XANES spectra taken at the maximum of Ru $L_{\alpha 1}$ emission line for the whole $Ca_3Mn_{2-x}Ru_xO_7$ ($0.05 \leq x \leq 0.9$) samples at room temperature, k^2-weighted EXAFS oscillations in k-space as a function of Ru concentration (x) at Mn K and Ru K edges, and detailed EXAFS analysis for the $Ca_3Mn_{2-x}Ru_xO_7$ ($0.1 \leq x \leq 0.7$) series at the Mn and Ru K-edges (PDF)

■ AUTHOR INFORMATION

Corresponding Authors

Gloria Subías − *Instituto de Nanociencia y Materiales de Aragón (INMA), CSIC-Universidad de Zaragoza, Zaragoza 50009, Spain; Departamento de Física de la Materia Condensada, Universidad de Zaragoza, Zaragoza 50009, Spain;* orcid.org/0000-0002-9029-1977; Email: gloria@unizar.es

Javier Blasco − *Instituto de Nanociencia y Materiales de Aragón (INMA), CSIC-Universidad de Zaragoza, Zaragoza 50009, Spain; Departamento de Física de la Materia Condensada, Universidad de Zaragoza, Zaragoza 50009, Spain;* orcid.org/0000-0002-9706-3272; Email: jbc@unizar.es

Authors

Vera Cuartero − *Instituto de Nanociencia y Materiales de Aragón (INMA), CSIC-Universidad de Zaragoza, Zaragoza 50009, Spain; Departamento de Ciencia y Tecnología de Materiales y Fluidos, EINA, Universidad de Zaragoza, Zaragoza 50018, Spain*

Javier Herrero-Martín − *CELLS-ALBA Synchrotron, Barcelona 08290, Spain*

Sara Lafuerza − *Instituto de Nanociencia y Materiales de Aragón (INMA), CSIC-Universidad de Zaragoza, Zaragoza 50009, Spain; Departamento de Física de la Materia Condensada, Universidad de Zaragoza, Zaragoza 50009, Spain*

Viktoriia A. Saveleva − *ESRF − The European Synchrotron Radiation Facility, Grenoble 38000, France;* orcid.org/0000-0002-8221-4576

Pieter Glatzel − *ESRF − The European Synchrotron Radiation Facility, Grenoble 38000, France;* orcid.org/0000-0001-6532-8144

Raffaella Torchio − *ESRF − The European Synchrotron Radiation Facility, Grenoble 38000, France*

https://doi.org/10.1021/acsomega.4c04334
ACS Omega 2024, 9, 41396−41407

Olivier Mathon − *ESRF − The European Synchrotron Radiation Facility, Grenoble 38000, France*

Complete contact information is available at: https://pubs.acs.org/10.1021/acsomega.4c04334

Author Contributions

The manuscript was written through contributions of all authors. All authors have given approval to the final version of the manuscript.

Notes

The authors declare no competing financial interest.

■ ACKNOWLEDGMENTS

For financial support, we thank grants PID2021-124734OB-C21 and -C22 funded by MCIN/AEI/10.13039/501100011033 and, as appropriate, by "ERDF A way of making Europe" and Gobierno de Aragón (project E12-23R). We acknowledge the ALBA synchrotron (proposal n° 2020094610) and the European Synchrotron Radiation Facility (doi.org/10.15151/ESRF-ES-514140874) for granting beam time and the beamline staff for providing the support to perform the measurements.

■ REFERENCES

(1) Benedek, N. A.; Fennie, C. J. Hybrid Improper Ferroelectricity: A Mechanism for Controllable Polarization-Magnetization Coupling. *Phys. Rev. Lett.* **2011**, *106*, 107204.

(2) Oh, Y. S.; Luo, X.; Huang, F. T.; Wang, Y.; Cheong, S.-W. Experimental demonstration of hybrid improper ferroelectricity and the presence of abundant charged walls in $(Ca,Sr)_3Ti_2O_7$ crystals. *Nat. Mater.* **2015**, *14*, 407−413.

(3) Liu, X. Q.; Wu, J. W.; Shi, X. X.; Zhao, H. J.; Zhou, H. Y.; Qiu, R. H.; Zhang, W. Q.; Chen, X. M. Hybrid improper ferroelectricity in Ruddlesden-Popper $Ca_3(Ti,Mn)_2O_7$ ceramics. *Appl. Phys. Lett.* **2015**, *106*, 202903.

(4) Wang, Y.; Huang, F.-T.; Luo, X.; Gao, B.; Cheong, S.-W. The First Room-Temperature Ferroelectric Sn Insulator and Its Polarization Switching Kinetics. *Adv. Mater.* **2017**, *29* (2), 1601288.

(5) Lobanov, M. V.; Greenblatt, M.; Caspi, E. N.; Jorgensen, J. D.; Sheptyakov, D. V.; Toby, B. H.; Botez, C. E.; Stephens, P. W. Crystal and magnetic structure of the $Ca_3Mn_2O_7$ Ruddlesden-Popper phase: neutron and synchrotron x-ray diffraction study. *J. Phys.: condens. Matter* **2004**, *16*, 5339−5348.

(6) Sahlot, P.; Awasthi, A. M. Uncompensated-spins induced weak ferromagnetism in $Ca_3Mn_2O_7$: Magneto-conductive and dual magneto-capacitive effects. *J. Magn. Magn. Mater.* **2020**, *493*, 165732.

(7) Fawcett, I. D.; Kim, E.; Greenblatt, M.; Croft, M.; Bendersky, L. A. Properties of the electron doped layered manganates $La_{2-2x}Ca_{1+2x}Mn_2O_7$ ($0.6 \leq x \leq 1.0$). *Phys. Rev. B* **2000**, *62*, 6485−6495.

(8) Zhang, X.; Liu, W.; Han, Y.; Huang, C.; Wu, P.; Zhou, W.; Gao, J.; Rao, G.; Wang, S. Novel optical and magnetic properties of Li-doped quasi-2D Manganite $Ca_3Mn_2O_7$ particles. *J. Mater. Chem. C* **2017**, *5*, 7011−7019.

(9) Lobanov, M. V.; Li, S.; Greenblatt, M. Structural, Magnetic, and Transport Properties of the Two Electron-Doped Ruddlesden−Popper Manganites Ca 3 - x Th x Mn 2 O 7. *Chem. Mater.* **2003**, *15* (6), 1302−1308.

(10) Sahu, R. K.; Mohammad, Q.; Rao, M. L.; Manoharan, S. S.; Nigam, A. K. Ruthenium-induced enhanced magnetization and metal−insulator transition in two-dimensional layered manganites. *Appl. Phys. Lett.* **2002**, *80* (1), 88−90.

(11) Yuan, K.; Zhang, H.; Gu, Q.; Xiao, T.; Li, Z.; Wong-Ng, W. K.; Zhou, W.; Wang, C.; Wang, S.; Liu, W. Enhanced magnetism in Ru-doped hybrid improper perovskite $Ca_3Mn_2O_7$ via experimental and first-principles study. *J. Am. Ceram. Soc.* **2023**, *106*, 2455−2465.

(12) Wu, X.; Wang, S.; Wong-Ng, W.; Gu, Q.; Jiang, Y.; Wang, C.; Ma, S.; Liu, W. Novel optical properties and induced magnetic moments in Ru-doped hybrid improper ferroelectric $Ca_3Ti_2O_7$. *J. Adv. Ceram.* **2021**, *10*, 120−128.

(13) Blasco, J.; Rodríguez-Velamazán, J. A.; García-Muñoz, J. L.; Cuartero, V.; Lafuerza, S.; Subías, G. Structural and magnetic properties of $Ca_3Mn_{2-x}Ru_xO_7$ ($0 \leq x \leq 0.9$). *Phys. Rev. B* **2022**, *106*, 134403.

(14) Lafuerza, S.; Retegan, M.; Detlefs, B.; Chatterjee, R.; Yachandra, V.; Yano, J.; Glatzel, P. New reflections on hard X-ray photon-in/photon-out spectroscopy. *Nanoscale* **2020**, *12*, 16270−16284.

(15) García, J.; Subías, G.; Cuartero, V.; Herrero-Martín, J. On the correlation between the X-ray absorption chemical shift and the formal valence state in mixed-valence manganites. *J. Synchrotron Rad.* **2010**, *17*, 386−392.

(16) Barla, A.; Nicolás, J.; Cocco, D.; Valvidares, S. M.; Herrero-Martín, J.; Gargiani, P.; Moldes, J.; Ruget, C.; Pellegrin, E.; Ferrer, S. Design and performance of BOREAS, the beamline for resonant X-ray absorption and scattering experiments at the ALBA synchrotron light source. *J. Synchrotron Rad.* **2016**, *23*, 1507−1517.

(17) Rovezzi, M.; Harris, A.; Detlefs, B.; Bohdan, T.; Svyazhin, A.; Santambrogio, A.; Degler, D.; Baran, R.; Reynier, B.; Noguera Crespo, P.; et al. TEXS: in-vacuum tender X-ray emission spectrometer with 11 Johansson crystal analyzers. *J. Synchrotron Rad.* **2020**, *27*, 813−826.

(18) Glatzel, P.; Harris, A.; Marion, P.; Sikora, M.; Weng, T.-C.; Guilloud, C.; Lafuerza, S.; Rovezzi, M.; Detlefs, B.; Ducotté, L. The five-analyzer point-to-point scanning crystal spectrometer at ESRF ID26. *J. Synchrotron Rad.* **2021**, *28*, 362−371.

(19) Campbell, J.; Papp, T. Widths of the atomic K-N7 levels. *At. Data Nucl. Data Tables* **2001**, *77*, 1−56.

(20) Mathon, O.; Beteva, A.; Borrel, J.; Bugnazet, D.; Gatla, S.; Hino, R.; Kantor, I.; Mairs, T.; Munoz, M.; Pasternak, S.; Perrin, F.; Pascarelli, S. The time-resolved and extreme conditions XAS (TEXAS) facility at the European Synchrotron Radiation Facility: the general-purpose EXAFS bending-magnet beamline BM23. *J. Synchrotron Rad.* **2015**, *22*, 1548−1554.

(21) Ravel, B.; Newville, M. ATHENA, ARTEMIS, HEPHAESTUS: data analysis for X-ray absorption spectroscopy using IFEFFIT. *J. Synchrotron Rad.* **2005**, *12*, 537−541.

(22) Subías, G.; García, J.; Sánchez, M. C.; Blasco, J.; Proietti, M. G. Soft x-ray absorption spectroscopy (Mn $L_{2,3}$ and O K) in mixed valence manganites. *Surf. Rev. Lett.* **2002**, *9*, 1071−1078.

(23) Thole, B. T.; Carra, P.; Sette, F.; van der Laan, G. X-ray circular dichroism as a probe of orbital magnetization. *Phys. Rev. Lett.* **1992**, *68*, 1943.

(24) Carra, P.; Thole, B. T.; Altarelli, M.; Wang, X. D. X-ray circular dichroism and local magnetic fields. *Phys. Rev. Lett.* **1993**, *70*, 694.

(25) Teramura, Y.; Tanaka, A.; Jo, T. Effect of Coulomb Interaction on the X-Ray Magnetic Circular Dichroism Spin Sum Rule in 3d Transition Elements. *J. Phys. Soc. Jpn.* **1996**, *65*, 1053−1055.

(26) Guo, H.; Gupta, A.; Varela, M.; Pennycook, S. J.; Zhang, J. Local valence and magnetic characteristics of La_2NiMnO_6. *Phys. Rev. B* **2009**, *79*, 172402.

(27) Edmonds, K. W.; Farley, N. R. S.; Johal, T. K.; van der Laan, G.; Campion, R. P.; Gallagher, B. L.; Foxon, C. T. Ferromagnetic moment and antiferromagnetic coupling in (Ga,Mn)As thin films. *Phys. Rev. B* **2005**, *71*, 064418.

(28) Sokolov, D. A.; Kikugawa, N.; Helm, T.; Borrmann, H.; Burkhardt, U.; Cubitt, R.; White, J. S.; Ressouche, E.; Bleuel, M.; Kummer, K.; Mackenzie, A. P.; Rößler, U. K. Metamagnetic texture in a polar antiferromagnet. *Nat. Phys.* **2019**, *15*, 671−677.

(29) García, J.; Subías, G.; Cuartero, V.; Herrero-Martin, J. On the correlation between the X-ray absorption chemical shift and the formal valence state in mixed-valence manganites. *J. Synchrotron Rad.* **2010**, *17*, 386−392.

(30) Cuartero, V.; Lafuerza, S.; Rovezzi, M.; García, J.; Blasco, J.; Subías, G.; Jiménez, E. X-ray absorption and emission spectroscopy

study of Mn and Co valence and spin states in $TbMn_{1-x}Co_xO_3$. *Phys. Rev. B* **2016**, *94*, 155117.
(31) Bunau, O.; Joly, Y. Self-consistent aspects of x-ray absorption calculations. *J. Phys.: condens. Matter* **2009**, *21*, 345501.
(32) Petrykin, V.; Bastl, Z.; Franc, J.; Macounova, K.; Makarova, M.; Mukerjee, S.; Ramaswamy, N.; Spirovova, I.; Krtil, P. Local Structure of Nanocrystalline $Ru_{1-x}Ni_xO_{2-\delta}$ Dioxide and Its Implications for Electrocatalytic Behaviors: An XPS and XAS Study. *J. Phys. Chem. C* **2009**, *113*, 21657−21666.
(33) Kim, J.-Y.; Hwang, S.-H.; Kim, S.-J.; Demazeau, G.; Choy, J.-H.; Shimada, H. 4d Electronic structure analysis of ruthenium in the perovskite oxides by Ru K- and L-edge XAS. *J. Synchrotron Rad.* **2001**, *8*, 722−724.
(34) Hu, Z.; von Lips, H.; Golden, M. S.; Fink, J.; Kaindl, G.; de Groot, F. M. F.; Ebbinghaus, S.; Reller, A. Multiplet effects in the Ru $L_{2,3}$ x-ray-absorption spectra of Ru(IV) and Ru(V) compounds. *Phys. Rev. B* **2000**, *61*, 5262.
(35) Svyazhin, A.; Nalbandyan, V.; Rovezzi, M.; Chumakova, A.; Detlefs, B.; Guda, A. A.; Santambrogio, A.; Manceau, A.; Glatzel, P. Chemical Information in the L_3 X-ray Absorption Spectra of Molybdenum Compounds by High-Energy-Resolution Detection and Density Functional Theory. *Inorg. Chem.* **2022**, *61*, 869−881.
(36) Zhou, Q.; Kennedy, B. J.; Zhang, Z.; Jang, L.-Y.; Aitken, J. B. X-ray Absorption near Edge Structure and Crystallographic Studies of the Mixed Valence Oxides $CaRu_{1-x}Mn_xO_3$. *Chem. Mater.* **2009**, *21*, 4203−4209.
(37) Rehr, J. J.; Albers, R. C. Theoretical Approaches to X-ray Absorption Fine Structure. *Rev. Mod. Phys.* **2000**, *72*, 621−654.
(38) Subías, G.; García, J.; Blasco, J.; Sánchez, M. C.; Proietti, M. G. Mn local structure effects in charge-ordered mixed-valence $RE_{1-x}Ca_xMnO_3$ (RE: La, Tb) perovskites: a review of the experimental situation. *J. Phys.: condens. Matter* **2002**, *14*, 5017−5033.
(39) Sarma, D. D.; Mahadevan, P.; Saha-Dasgupta, T.; Ray, S.; Kumar, A. Electronic Structure of Sr_2FeMoO_6. *Phys. Rev. Lett.* **2000**, *85*, 2549−2552.
(40) Terai, K.; Yoshii, K.; Takeda, Y.; Fujimori, S. I.; Saitoh, Y.; Ohwada, K.; Inami, T.; Okane, T.; Arita, M.; Shimada, K.; et al. X-ray magnetic circular dichroism and photoemission studies of ferromagnetism in CaMn 1 − x Ru x O 3 thin films. *Phys. Rev. B* **2008**, *77* (11), 115128.
(41) Mishra, R.; Soliz, J. R.; Woodward, P. M.; Windl, W. Ca_2MnRuO_6: Magnetic order arising from chemical chaos. *Chem. Mater.* **2012**, *24*, 2757−2763.

https://doi.org/10.1021/acsomega.4c04334
ACS Omega 2024, 9, 41396−41407